# Spin structures and phase diagrams of the spin- $\frac{5}{2}$ triangular lattice antiferromagnet Na<sub>2</sub>BaMn(PO<sub>4</sub>)<sub>2</sub> under magnetic field

N. Biniskos , <sup>1,\*</sup> F. J. dos Santos , <sup>2,3,4,†</sup> M. Stekiel , <sup>5,‡</sup> K. Schmalzl , <sup>6</sup> E. Ressouche , <sup>7</sup> D. Sviták , <sup>1</sup> A. Labh , <sup>1</sup> M. Vališka, N. Marzari, and P. Čermák, and P. Čermák

> <sup>1</sup>Faculty of Mathematics and Physics, Department of Condensed Matter Physics, Charles University, Ke Karlovu 5, 121 16, Praha, Czech Republic

<sup>2</sup>PSI Center for Scientific Computing, Theory, and Data, 5232 Villigen PSI, Switzerland

<sup>6</sup>Jülich Centre for Neutron Science (JCNS) at Institut Laue Langeving (ILL), Forschungszentrum Jülich GmbH, 71 Avenue des Martyrs, F-38000 Grenoble, France

<sup>7</sup>Université Grenoble Alpes, CEA, IRIG, MEM, MDN, F-38000 Grenoble, France

<sup>8</sup>Theory and Simulation of Materials (THEOS), École Polytechnique Fédérale de Lausanne, 1015 Lausanne, Switzerland



(Received 20 August 2025; accepted 4 November 2025; published 24 November 2025)

We combine single-crystal neutron diffraction studies and Monte Carlo simulations to determine the spin structures and finite-temperature phase diagram of the spin-5/2 triangular-lattice antiferromagnet Na<sub>2</sub>BaMn(PO<sub>4</sub>)<sub>2</sub> in magnetic field. With the application of a magnetic field in two different directions, namely along the c axis and in the ab plane of the trigonal symmetry, we track the evolution of the spin structure through changes of the magnetic propagation vector. We account for these results with a minimal Heisenberg Hamiltonian that includes easy-axis anisotropy and weak, frustrated interlayer couplings in addition to intralayer exchange. Guided by representation analysis, we refine symmetry-allowed modes to the measured intensities and obtain the spin structures for all field-induced phases, which we compare quantitatively with simulated configurations. Taken together, our measurements and simulations show that frustrated interlayer exchange—rather than purely two-dimensional physics—organizes the unexpectedly rich field-induced phases of Na<sub>2</sub>BaMn(PO<sub>4</sub>)<sub>2</sub>.

# DOI: 10.1103/kszh-m6bf

# I. INTRODUCTION

Frustrated triangular-lattice antiferromagnets (TLAs) are considered as model systems in which exotic states can emerge. For example, the suppression of exchange interactions due to geometric frustration and a low quantum spin number (S = 1/2) can result in strong quantum spin fluctuations at low temperatures that stabilize a quantum spin liquid state [1]. Such states exhibit several appealing properties in condensed matter physics like quasiparticle fractionalization [2], long-range entanglement [3], and topological order [4]. Novel phases of matter and interesting physical properties are not restricted only to frustrated magnet systems in the quantum limit (low spin), but can also emerge in the classical limit  $(S \ge 1)$  [5–7] and by applying an external magnetic field [8–11].

In this context, the equilateral TLAs Na<sub>2</sub>BaM(PO<sub>4</sub>)<sub>2</sub> (with M = Co, Ni, Mn) are good candidate materials to explore phenomena related to quantum magnetism, since the

\*Contact author: nikolaos.biniskos@matfyz.cuni.cz

<sup>†</sup>Contact author: flaviano@cbpf.br

<sup>‡</sup>Contact author: m.stekiel@fz-juelich.de

substitution of the transition metal ion leads to drastic changes in the quantum spin number [12-14]. The ground state of the phosphate with the lowest spin (S = 1/2), Na<sub>2</sub>BaCo(PO<sub>4</sub>)<sub>2</sub>, is proposed to form a Y-like spin supersolid phase in zero magnetic field [15,16] and is considered an ideal material where a spin-1/2 easy-axis XXZ model can be applied [17]. In addition, the spin supersolidity is connected to a giant magnetocaloric effect which is observed during the demagnetization cooling process [15]. On the contrary, Na<sub>2</sub>BaNi(PO<sub>4</sub>)<sub>2</sub>, where S = 1, is assumed to exhibit a spin nematic supersolid ground state that can be modeled by a spin Hamiltonian including a single-ion anisotropic term and nearest-neighbor XXZ-type exchange interactions [18]. Although this scenario is primarily supported by field-induced behavior and magnon-pair condensation at low temperatures [18], the precise nature of the zero-field ground state remains debated [19]. Na<sub>2</sub>BaMn(PO<sub>4</sub>)<sub>2</sub> is expected to be the classical counterpart of the TLA series due to the high quantum spin number (S = 5/2) of the Mn<sup>+2</sup> ions [14]. Also, it is worth mentioning that all compounds within the series manifest multiple field-induced phase transitions [13,14,20]. Above a critical field applied along the c axis, a magnetization plateau appears in a finite range of the external magnetic field where the magnetization reaches 1/3 of the saturation

<sup>&</sup>lt;sup>3</sup>National Centre for Computational Design and Discovery of Novel Materials (MARVEL), 5232 Villigen PSI, Switzerland <sup>4</sup>Centro Brasileiro de Pesquisas Físicas (CBPF), Rua Dr. Xavier Sigaud 150, Urca, Rio de Janeiro - RJ, 22290-180, Brazil

<sup>&</sup>lt;sup>5</sup> Jülich Centre for Neutron Science (JCNS) at Heinz Maier-Leibnitz Zentrum (MLZ), Forschungszentrum Jülich GmbH, Lichtenbergstrasse 1, D-85747 Garching, Germany

magnetization  $M_{\rm sat}$ . Such 1/3-magnetization plateaus were first observed in GdPd<sub>2</sub>Al<sub>3</sub> [21] and later in other TLAs such as RbFe(MoO<sub>4</sub>)<sub>2</sub> [22] and Ba<sub>3</sub>MnNb<sub>2</sub>O<sub>9</sub> [9]. While for Na<sub>2</sub>BaMn(PO<sub>4</sub>)<sub>2</sub> the magnetic structure at zero field was recently investigated with neutron powder diffraction measurements [23], the spin configurations of the field-induced phases and a minimal model Hamiltonian that describes the magnetic ground state remain unknown.

In this article, we report the synthesis of high quality crystals of Na<sub>2</sub>BaMn(PO<sub>4</sub>)<sub>2</sub> and unpolarized single-crystal neutron diffraction measurements. We investigated the fieldinduced phase transitions by recording magnetic reflections as a function of temperature (T) in different magnetic fields (H), applied along the c axis and in the ab plane of trigonal symmetry. By identifying the critical fields obtained from heat capacity and neutron diffraction measurements, we mapped the Na<sub>2</sub>BaMn(PO<sub>4</sub>)<sub>2</sub> phase diagrams for the two magnetic field directions. With a combination of spin dynamics and Monte Carlo simulations we attempt to determine the magnetic ground state of the system, reproduce the phase diagrams, and track the changes in the spin structure versus the applied magnetic field. In order to compare qualitatively the orientation of the ordered moments in the various fieldinduced transitions, we refine the obtained magnetic structures based on the integrated intensities of the magnetic reflections.

#### II. METHODS

### A. Experimental details

Na<sub>2</sub>BaMn(PO<sub>4</sub>)<sub>2</sub> single crystals were grown by the high temperature flux method [12,14] and were characterized with single crystal x-ray diffraction and specific heat measurements. Single crystal x-ray diffraction measurements were performed on a Rigaku XtaLAB Synergy-S diffractometer, using a Mo x-ray source providing a monochromatic beam with a wavelength of 0.71 Å and a two-dimensional HyPix-Arc 150° detector. The observed reflections were indexed and integrated using the data reduction program CRYSALISPRO [24]. The structure solution and refinement was performed with SHELX [25]. Heat capacity was measured on a Quantum Design Physical Property Measurement System (PPMS) equipped with the heat capacity option. Data were collected on a single crystal of Na<sub>2</sub>BaMn(PO<sub>4</sub>)<sub>2</sub> with a mass of about 0.6 mg, employing both the semiadiabatic time-relaxation technique and the long-pulse method described in Ref. [26].

A parallelepiped Na<sub>2</sub>BaMn(PO<sub>4</sub>)<sub>2</sub> single crystal with mass 37.7 mg was mounted on a copper sample holder and was oriented in the (hh0)/(00l) scattering plane of the trigonal lattice. In this article, we use the hexagonal coordinate system and the scattering vector  $\mathbf{Q}$  is expressed in  $\mathbf{Q} = (Q_h, Q_k, Q_l)$  given in reciprocal lattice units (r.l.u.). The relation between  $\mathbf{Q}$  and the propagation vector  $\mathbf{k}$  is given by  $\mathbf{Q} = \mathbf{G} + \mathbf{k}$ , where  $\mathbf{G}$  is at the  $\Gamma$  point of the reciprocal lattice.

Single-crystal neutron diffraction measurements were carried out at the Institut Laue-Langevin (ILL), in Grenoble, France. Data were obtained on the two-axis thermal neutron diffractometer D23 [27]. A copper monochromator provided an unpolarized neutron beam with a wavelength of 1.282 Å. In order to reach sub-kelvin temperatures, the sample holder

was attached to the mixing chamber of a dilution stick. To investigate the evolution of the spin structure under magnetic field, measurements were performed in two geometries: with a 15 T vertical field magnet, providing magnetic field within the *ab* plane, and with a 3.8 T horizontal field magnet, providing field along the *c* axis. In both geometries, data at zero field were collected and combined to refine the zero-field magnetic structures at 600 and 1200 mK. The various spin structures were refined using Mag2POL software [28].

#### **B.** Theoretical framework

The effective interactions between the magnetic moments of the Mn sites of  $Na_2BaMn(PO_4)_2$  were modeled using a classical Heisenberg Hamiltonian:

$$\mathcal{H} = -\sum_{ij} J_{ij} \mathbf{S}_i \cdot \mathbf{S}_j - k^c \sum_i \left( S_i^c \right)^2. \tag{1}$$

Here,  $J_{ij}$  are the magnetic exchange interaction parameters and  $k^c$  corresponds to the single-ion anisotropy along the c axis. Negative J values characterize antiferromagnetic (AFM) coupling. We will discuss the choice of parameters in detail in Sec. III, together with the experimental findings.

For this model, the ground state spin configuration was determined through spin dynamics by solving the Landau-Lifshitz-Gilbert equation using the Spirit package [29]. The spin-wave spectrum was determined using linear spin-wave theory for noncollinear magnets [30]. Finally, Monte Carlo simulations were employed to determine the mechanical statistical properties of the system using the Vampire package [31,32]. We used a  $3 \times 3 \times 5$  macrocell with periodic boundaries and an equilibration time of 5000 Monte Carlo steps, and statistical averaging also over 5000 steps.

# III. RESULTS AND DISCUSSION

### A. Crystal structure

The crystal structure of the manganese phosphate  $Na_2BaMn(PO_4)_2$  was determined by single crystal x-ray diffraction at room temperature. The compound crystallizes in the trigonal lattice with space group  $P\overline{3}$  (147) and lattice parameters a=5.37304(4) Å and c=7.0944(10) Å. The structure is presented in Fig. 1 and details of the refinement are given in Table I. The building blocks of the crystal structure are regular  $MnO_6$  octahedra and  $PO_4$  tetrahedra with interstitial Na and Ba ions.  $MnO_6$  octahedra are corner connected through  $PO_4$  groups and form layers stacked along the [001] direction. The Na and Ba ions fill the interstitial positions and bond adjacent MnO layers.

All measured crystals exhibit merohedral twinning with apparent  $P\bar{3}m1$  symmetry, where the mirror plane  $m_{100}$  defines the twinning law. Regarding the atomic positions, the difference in assigning either space group concerns only the oxygen at the 6i site, where constraints of the  $P\bar{3}m1$  space group give  $y(O_{6i}) = \frac{1}{2}x(O_{6i})$ , while the  $P\bar{3}$  space group sets the y coordinate free. The refinement with the  $P\bar{3}m1$  space group results in five times larger displacement parameters of  $O_{6i}$  and three times higher R factors than the refinement with the  $P\bar{3}$  structure. Releasing the constraints and refining the structure with  $P\bar{3}$  space group yields excellent quality factors

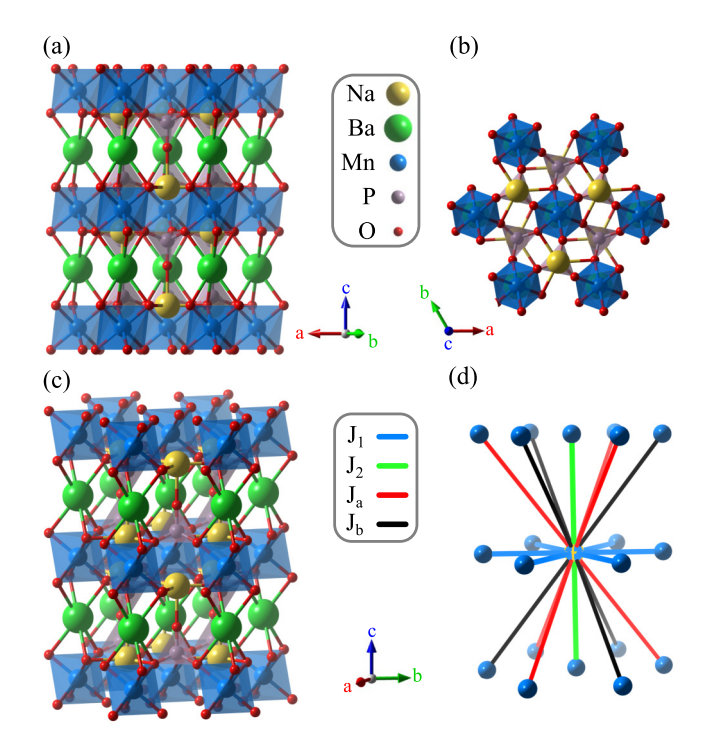


FIG. 1. Crystal structure of  $Na_2BaMn(PO_4)_2$  as determined by single crystal x-ray diffraction. (a) View along the in-plane direction, highlighting the layered structure. (b) View along the c axis. (c),(d) General view highlighting the connectivity of Mn ions, where (d) shows the Mn–Mn bonds used in theoretical modeling of the spin interactions, in-plane  $J_1$  (bond length is 5.37 Å), out-of-plane  $J_2$  (7.094 Å), and diagonal out-of-plane  $J_a$  and  $J_b$  (both 8.9 Å). Even though the bond length for  $J_a$  and  $J_b$  is the same, the bonds are not equivalent in the  $P\bar{3}$  space group.

and gives the twinning ratio of 70:30. The y coordinate of position  $O_{6i}$  differs significantly from the  $y = \frac{1}{2}x$  constraint  $(y \approx 0.24 \text{ vs constrained } y \approx 0.18)$  and corresponds to the rotation of the MnO<sub>6</sub> octahedra by an angle of 9.9° from their positions in the  $P\bar{3}m1$  space group. The twinning is consistent with the recently reported high temperature transition in Na<sub>2</sub>BaMn(PO<sub>4</sub>)<sub>2</sub> [33] and explains the inconsistencies between the reports on the  $P\bar{3}$  [23,33–35] and  $P\bar{3}m1$  [14,36]

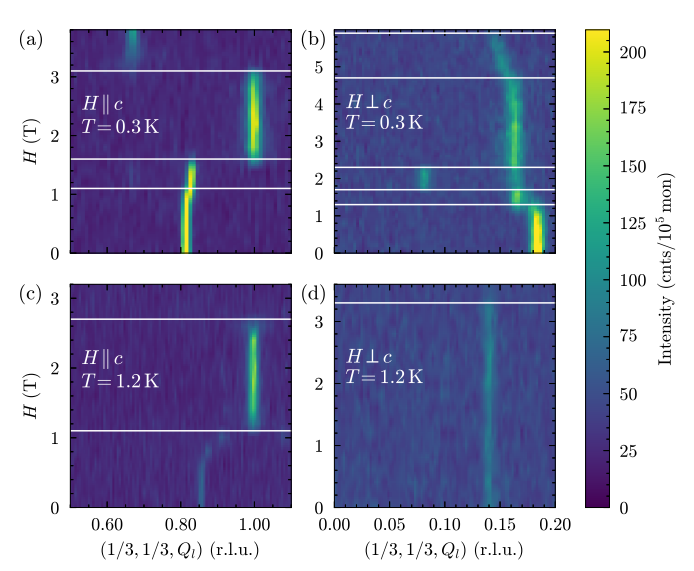


FIG. 2. Color-coded intensity plots of single crystal neutron diffraction data of Na<sub>2</sub>BaMn(PO<sub>4</sub>)<sub>2</sub> collected at 300 and 1200 mK as a function of  $\mathbf{Q} = (1/3, 1/3, Q_l)$  and applied magnetic field along (a), (c) the c axis and (b), (d) in the ab plane. White horizontal lines represent the identified phase boundaries.

space groups. It is worth mentioning that a similar twinning scheme was recently considered for Na<sub>2</sub>BaCo(PO<sub>4</sub>)<sub>2</sub> [37].

#### B. Field-induced phase transitions

Zero magnetic field heat capacity measurements on single crystals [14] and neutron powder diffraction experiments [23] revealed that long-ranged AFM order appears in Na<sub>2</sub>BaMn(PO<sub>4</sub>)<sub>2</sub> at low temperatures. The system at zero field undergoes two successive magnetic transitions at  $T_{N_2} \approx 1.28$  K (AFM2) and  $T_{N_1} \approx 1.13$  K (AFM1) into antiferromagnetic phases that are indexed with the modulation vector  $\mathbf{k}_{\text{AFM2}} = (1/3, 1/3, 0.139)$  and  $\mathbf{k}_{\text{AFM1}} = (1/3, 1/3, 0.187)$ , respectively [23]. Consistently our neutron data in Fig. 2 indicate the occurrence of spin ordering at zero field for  $T < T_{N_1}$  with  $\mathbf{k}_{\text{AFM1}} = (1/3, 1/3, 0.187)$  and for  $T_{N_1} \leqslant T \leqslant T_{N_2}$  with  $\mathbf{k}_{\text{AFM2}} = (1/3, 1/3, 0.147)$ . The significant difference in  $\mathbf{k}_{\text{AFM2}}$ 

TABLE I. Crystal structure parameters of Na<sub>2</sub>BaMn(PO<sub>4</sub>)<sub>2</sub> based on the refinement of single crystal x-ray diffraction data at 296 K. The space group is  $P\bar{3}$  and the lattice parameters are a=5.37304(4) Å and c=7.0944(10) Å. The number of measured, independent, and observed reflections are 304432, 2564, and 2444, respectively. The reflection merge factor is  $R_{\rm int}=6.45$  and observed reflections are with  $I>2\sigma(I)$ . The refinement was performed on  $F^2$  with  $R_{\rm obs}=1.63$  and  $wR_{\rm obs}=4.92$ . The columns contain the name of the elements, Wyckoff site symbols, positions in crystal coordinates, and displacement parameters, respectively. Numbers without errors are restricted by site symmetry.

Atom	Site		Position			U (Å <sup>2</sup> )			
		x	у	z	$U_{11} = U_{22}$	U <sub>33</sub>	U <sub>12</sub>	$U_{23} = -U_{13}$	$U_{eq}$
Mn	1 <i>a</i>	0	0	0	0.00758(3)	0.00663(4)	0.00379(1)	0	0.00726(2)
Ba	1 <i>b</i>	0	0	$\frac{1}{2}$	0.01385(2)	0.00636(2)	0.00693(1)	0	0.01135(2)
Na	2d	$\frac{1}{3}$	$\frac{2}{3}$	0.18600(14)	0.01547(13)	0.0217(3)	0.00773(7)	0	0.01755(10)
P	2d	$\frac{2}{3}$	$\frac{1}{3}$	0.26286(4)	0.00649(4)	0.00636(6)	0.00324(2)	0	0.00645(3)
O	2d	$\frac{2}{3}$	$\frac{1}{3}$	0.47708(12)	0.01831(18)	0.00663(17)	0.00915(9)	0	0.01441(11)
O	6i	0.36193(12)	0.23574(15)	0.18706(10)	0.00845(12)	0.01453(18)	0.00543(12)	-0.00322(15)	0.01347(7)

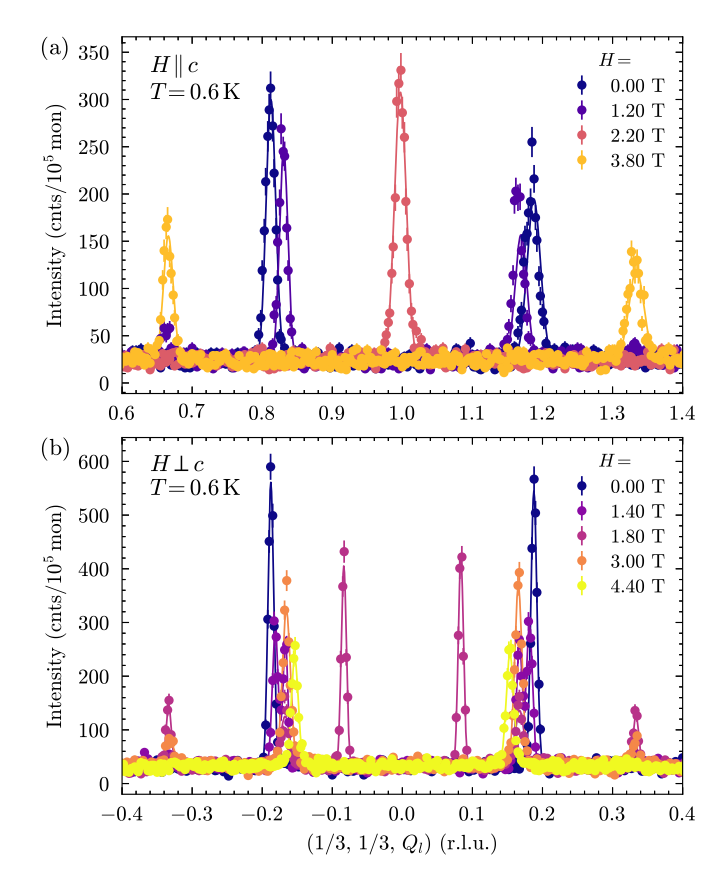


FIG. 3. Representative reciprocal space scans at  $Q = (1/3, 1/3, Q_l)$  measured at 600 mK, under different applied fields applied along (a) the c axis and (b) in the ab plane. Lines represent fits with Gaussian functions on top of a constant background.

between our results and Ref. [23] is ascribed to the temperature dependence of the propagation vector within this phase. We also note that due to the blockage of the bulky horizontal magnet several magnetic reflections constrained in the (hhl) plane are not accessible. Therefore, data could not be obtained for  $-0.5 < Q_l < 0.5$  r.l.u. for  $\boldsymbol{H} \parallel \hat{\boldsymbol{c}}$  [see Figs. 2(a) and 2(c)].

Based on  $\chi_{ac}$  magnetic susceptibility measurements on single-crystal samples [14], when a magnetic field is applied parallel or perpendicular to the c axis of the trigonal symmetry, multiple field-induced phase transitions occur, whose spin configurations are still unexplored to our knowledge. Therefore, a first essential step for determining the spin arrangement of the various spin structures is to index their magnetic propagation vector. To this aim, we performed reciprocal space scans for magnetic fields  $H \parallel \hat{c}$  and  $H \perp \hat{c}$  and the results are presented in Fig. 2 and Fig. 3. The AFM order is characterized by magnetic reflections arising as satellites to the nuclear Bragg reflections with modulation vector  $(1/3, 1/3, k_z)$ , where  $k_z$  changes as a function of the applied field direction and magnitude.

The evolution of the magnetic order at  $T=300 \,\mathrm{mK}$  for  $H \parallel \hat{c}$  is depicted in Fig. 2(a) where for critical fields  $H > H_{c_1}^{\parallel}$  the system shows commensurate ordering. Three different phases can be distinguished up to the maximum investigated magnetic field of 3.8 T: (i) for  $H_{c_1}^{\parallel} \leq H < H_{c_2}^{\parallel}$  the

magnetic wave vector slightly shifts and becomes (1/3, 1/3, 1/6) with a second less intense magnetic peak appearing at (1/3, 1/3, 1/3), (ii) for  $H_{c_2}^{\parallel} \leq H \leq H_{c_3}^{\parallel}$  the system enters into the 1/3 plateau phase [14] and this is accompanied by a first sudden change in k which is now located at (1/3, 1/3, 0) [up-up-down (UUD) phase], and (iii) a second abrupt jump results to k = (1/3, 1/3, 1/3) for  $H_{c_3}^{\parallel} < H \leq H_{c_2}^{\parallel}$ . In contrast, at T = 1200 mK for  $H_{c_1}^{\parallel} \leq H < H_{c_2}^{\parallel}$ , a continuous diminution of the magnetic peak intensity and a shift of k towards the K point are observed [see Fig. 2(c)]. When the system is tuned into the UUD phase, a strong enhancement of the peak intensity is detected before reaching the spin-polarized (SP) state.

Figure 2(b) shows the reciprocal space scans at Q = (1/3,1/3,  $Q_l$ ) for  $\mathbf{H} \perp \hat{\mathbf{c}}$  at T = 300 mK. Based on the scattering geometry given in Sec. II the magnetic field points along the [110] direction of the trigonal symmetry. With increasing magnetic field we observed the following: (i) in the narrow range  $H_{c_1}^{\perp} \leqslant H < H_{c_2}^{\perp}$  the zero-field AFM1 might be coexisting with another phase that can be indexed with  $\mathbf{k} = (1/3, 1/3, 1/12), \text{ (ii) for } H_{c_2}^{\perp} \leqslant H < H_{c_3}^{\perp} \text{ the } (1/3, 1/3),$ 1/3, 1/12) reflection becomes very sharp, while three additional less intense peaks appear in commensurate positions with  $k_7' = 1/6$ , 1/3, and 5/12, (iii) for  $H_{c_3}^{\perp} \leq H < H_{c_4}^{\perp}$  the magnetic peak is located at (1/3, 1/3, 1/6) and a second weaker at (1/3, 1/3, 1/3), and (iv) for  $H_{c_4}^{\perp} \leq H < H_{SP}^{\perp}$  the system becomes incommensurate with  $k_z$  changing continuously with field, before reaching the spin-polarized state. It is worth mentioning that at T = 1200 mK no field-induced phase transition is detected until the system enters the SP state [see Fig. 2(d)]. Representative Q scans for every phase showing the main and secondary magnetic peak positions for the two field directions are summarized in Fig. 3.

#### C. Temperature and magnetic field phase diagrams

From the peak positions in the heat capacity data and the changes of the propagation vector we constructed the temperature and magnetic field phase diagrams shown in Fig. 4. The phase boundaries for the spin polarized state for the two field directions are in agreement with a previous report [14]; however, our data suggest more complex H-T phase diagrams. For  $H \parallel \hat{c}$ , we evidence the formation of two pocket phases; a narrow between the AFM1 and the UUD phase, and AFM2. For  $H \perp \hat{c}$  there is an absence of a phase transition for AFM2, a narrow region for  $T < T_{N_1}$  where the AFM1 incommensurate ground state coexists with a commensurate phase, and a phase transition between a commensurate and incommensurate phase at higher magnetic fields.

The existence of a 1/3 plateau (UUD phase) is reported also in other classical TLA systems with S = 5/2, e.g., Rb<sub>4</sub>Mn(MoO<sub>4</sub>)<sub>3</sub> [38], Ba<sub>3</sub>MnNb<sub>2</sub>O<sub>9</sub> [9] (Mn<sup>+2</sup>), and RbFe(MoO<sub>4</sub>)<sub>2</sub> [22] (Fe<sup>+3</sup>). For classical systems the stability of the UUD phase in a finite temperature range indicates that thermal fluctuations are lifting the degeneracy of the ground state [39,40]; otherwise, their absence would result in the appearance of the UUD phase at a single point. Thermal fluctuations are responsible for lowering the free energy of the system by selecting the highest entropic state, where two spins are aligned parallel and the other spin antiparallel to

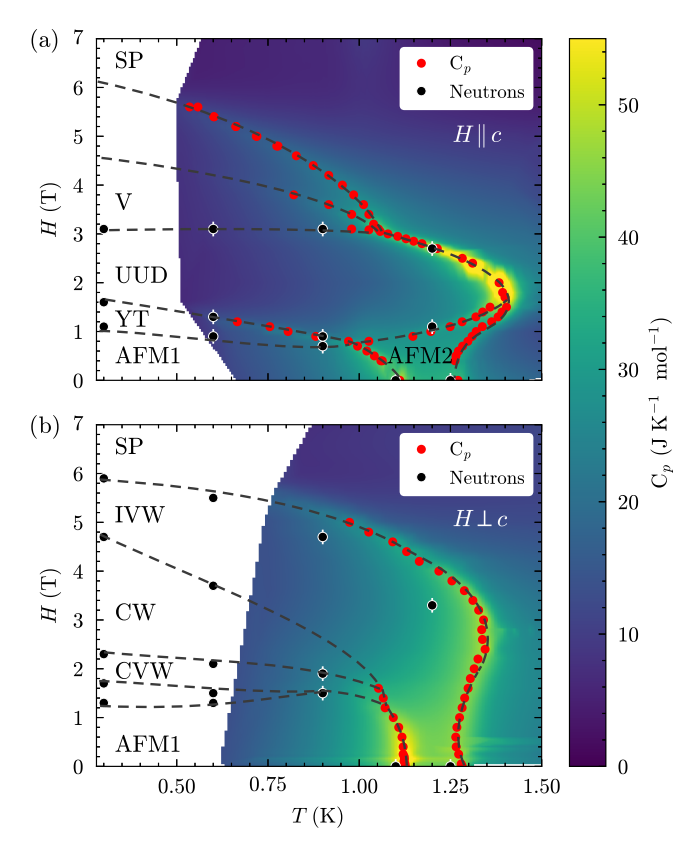


FIG. 4. Temperature and magnetic field phase diagrams of  $Na_2BaMn(PO_4)_2$  with magnetic field applied along (a) the c axis and (b) in the ab plane. Red and black circles indicate critical fields determined from specific heat (background heat map) and neutron diffraction measurements, respectively. Phase boundaries are marked by dashed gray lines and are guides for the eyes.

the direction of the external applied magnetic field. As the magnetic field further increases, a canted version of the UUD phase becomes stable (umbrella or V phase) [41,42].

# D. Spin structures under magnetic field

The spin structure models of Na<sub>2</sub>BaMn(PO<sub>4</sub>)<sub>2</sub> are based on the representation analysis of the modulation vector  $\mathbf{k} = (1/3, 1/3, k_z)$ , with the component  $k_z$  varying throughout the phase diagram, as summarized in Sec. III B. For all values of  $k_7$ , there are the same three irreducible representations (irreps) of the magnetic propagation vector group  $\Gamma_{\text{mag}} = \Gamma_1 \oplus \Gamma_2 \oplus \Gamma_3$ , which are presented in Table II.  $\Gamma_1$ mode is a collinear arrangement of moments along the c axis, with the up-up-down (UUD) amplitude pattern for zero phase and plus-minus-zero for phase  $\pi/4$ . The modulation along the c-axis direction given by  $k_z$  modulates the spin arrangement between these two patterns.  $\Gamma_2$  has magnetic moments coplanar in the (001) plane, with moments forming the 120° structure along Mn-Mn bonds and the  $k_z$  modulation rotates the moments around the c axis, showing right-handed helical modulation.  $\Gamma_3$  is the same as  $\Gamma_2$ , but the  $k_z$  modulation is left-handed. An explicit mode decomposition and notation are given in the Supplemental Material (see Eq. S1 [43]).

Before presenting the results there are three important points to address regarding our measurements. First,

TABLE II. Irreducible representations of the magnetic moments of Mn ions in Na<sub>2</sub>BaMn(PO<sub>4</sub>)<sub>2</sub>. Irreps are derived for the Wyck-off position 1*a* in the space group  $P\bar{3}$  and modulation vector  $\mathbf{k} = (1/3, 1/3, k_z)$ . Columns contain irreps symbols, normalized basis vectors, and description of the spin structures.

Irreps	Basis vector	Description
$\Gamma_1$	[0 0 1]	Collinear with the $c$ axis modulating between UUD and $+-0$
$\Gamma_2$	$[0.612\ 0\ 0]$ $-i[0.354\ 0.707\ 0]$	$120^{\circ}$ in <i>ab</i> plane, right-handed helical modulation along the <i>c</i> axis
$\Gamma_3$	$[0.612\ 0\ 0] + i[0.354\ 0.707\ 0]$	$120^{\circ}$ in $ab$ plane, left-handed helical modulation along the $c$ axis

unpolarized neutron diffraction cannot distinguish between opposing chiralities of the magnetic structure, that is, the difference between  $\Gamma_2$  and  $\Gamma_3$ , but can determine the ratio of these mode amplitudes. Therefore, the magnetic structure can be described with reference to the in-plane component ( $\Gamma_2$  and  $\Gamma_3$  mixing) and out-of-plane component ( $\Gamma_1$ ). Second, neutron diffraction cannot determine the global phase of the magnetic modulation, which is crucial to accurately depict the structure with a commensurate modulation vector. We have chosen the phase to best match the theoretical models presented in the next section. Finally, it is important to note that the refinement of the satellite reflection intensities allowed us to determine the antiferromagnetic component of the magnetic order. Under an applied magnetic field, there is an additional ferromagnetic component arising from magnetization that contributes to the nuclear reflections; however, determining its precise value from neutron diffraction measurements is unreliable. For depicting the magnetic structures under field we used the magnetization values determined in Ref. [14], also shown in Fig. 6. A comprehensive list of the refinement parameters, including mode amplitudes, ferromagnetic components, and global phases, is given in the Supplemental Material (see Table SII and goodness-of-fit plots in Fig. S2 [43]).

The spin arrangement at 600 mK and zero field (AFM1 phase) shows in-plane and out-of-plane components, as displayed in Fig. 5(a). The in-plane modes  $\Gamma_2$  and  $\Gamma_3$  sum up to a collinear component along the [120] direction, which in combination with the out-of-plane mode  $\Gamma_1$  results in a coplanar structure with Y arrangement of spin directions in the z = 0 layer. The incommensurability of the modulation vector changes the phase of the spin configuration along the [001] direction, resulting in cycloidal modulation of Mn spins with  $\approx$ 60° interlayer phase shift and effective rotation of the Y configuration along the c-axis direction. The average magnitude of the individual moments is  $3.70(8)\mu_B$ . Magnetic ordering at 1200 mK and zero field (AFM2 phase) is pure  $\Gamma_1$  mode, that is, a collinear UUD structure along the c axis, as shown in Fig. 5(e). The absolute value of the magnetic moment is reduced to  $\mu = 2.07(1)\mu_{\rm B}$  and the structure resembles the 600 mK arrangement dynamically disordered within the ab plane. Our refinements in zero field match those reported in Ref. [23], where the authors determined the magnetic structures based on neutron powder diffraction of Na<sub>2</sub>BaMn(PO<sub>4</sub>)<sub>2</sub>

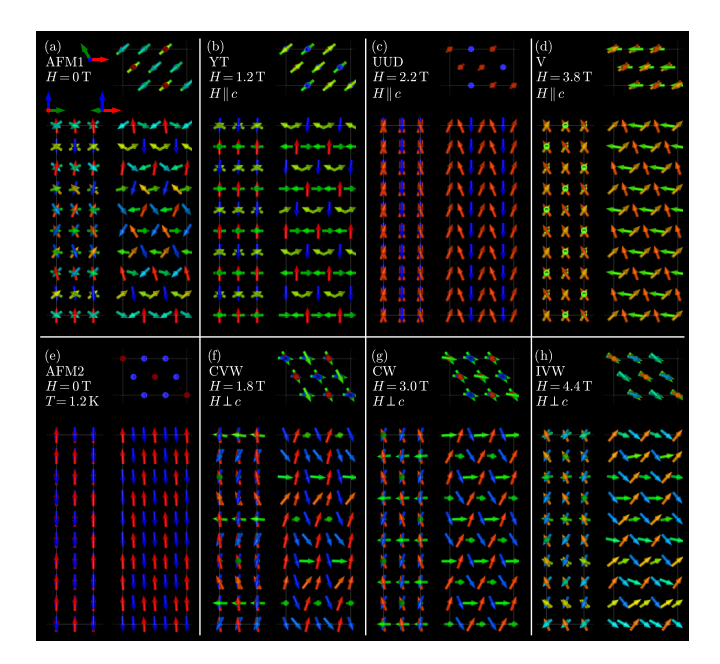


FIG. 5. Magnetic structures of Na<sub>2</sub>BaMn(PO<sub>4</sub>)<sub>2</sub> based on single crystal neutron diffraction measurements under applied field. All structures are determined at 600 mK except the AFM2 phase (e). Each structure is depicted from the directions along the c, a, and  $a^*$ axis. Axes coordinates for these views are depicted only in (a) showing  $a_1$ ,  $a_2$ , and c axis in red, green, and blue, respectively. (a) At zero field and 600 mK, the spin configuration is incommensurate, coplanar with Y arrangement of spins and components along the c axis and [120] direction. (e) At 1200 mK it is collinear along the c axis, with moments in an up-up-down pattern. When a magnetic field is applied along the c axis, spins gradually align with the field forming (b) alternating YT layers at 1.2 T, (c) the UUD phase at 2.2 T, and (d) the umbrella V arrangement at 3.8 T. For the field applied along the [110] direction the spins also gradually align along the field, with (f) commensurately alternating V-W layers at 1.8 T, (g) commensurately stacked W layers at 3 T, and (h) incommensurately modulated V-W layers at 4.4 T. A detailed description of all phases is given in the main text; numerical values used to render all panels are listed in the Supplemental Material in Table SII [43].

at 67 mK and 1.25 K, with small differences in the modulation vector.

The field applied along the c axis breaks the incommensurate modulation of the spin arrangement and introduces intermediate, commensurate phases before field polarizing the spins [see Figs. 5(b)-5(d)]. At 1.2 T (YT phase) the refinement resembles the ground state Y configuration with spins slightly rotated along the field direction. The modulation along the c axis alternates between the distorted Y configuration and T configuration, where the latter depicts two spins arranged antiferromagnetically within the ab plane and one spin along the c axis. Note that the refinement at 1.2 T was poor compared to the other refinements [see Fig. S2(b) in the Supplemental Material [43] and should be treated as a rough approximation. Next, at 2.2 T spins arrange in the UUD configuration along the c axis with a small in-plane component (UUD phase). The in-plane component is collinear with the [120] direction and five times smaller than the c-axis component. Finally, at 3.8 T the spins rearrange to an umbrella configuration

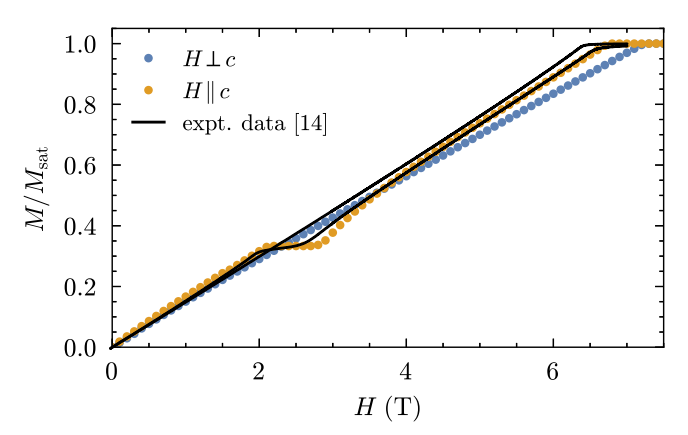


FIG. 6. Magnetization as a function of applied fields along and perpendicular to the easy axis. Experimental data based on Ref. [14]. Simulation (color circles) including single-ion anisotropy with easy axis along c. The length of the plateau is proportional to the single-ion anisotropy.

(V phase), where all spins have positive components along the field, while the in-plane component spreads them around in a  $120^{\circ}$  configuration.

With the field applied in plane, all measured phases show almost coplanar arrangement, as the dominant component is  $\Gamma_1$  mode with c-axis component and uniform magnetization aligning the moments toward the [110] direction. As a consequence, the spins are lying within the (110) plane, that is, they have dominating components along the c axis and field direction [see Figs. 5(f)-5(h)]. At 1.8 T the spins arrange in alternating V and W layers, with opening along the applied field direction [110] (CVW phase). The V configuration is a superposition of UUD along the c axis and uniform magnetization along the applied field resulting in spins out of plane, while the W configuration describes one spin along the field direction and the other two spread up and down with respect to the first one. When increasing the field to 3 T there are only W layers with commensurate modulation along the c axis and opening of  $\approx 120^{\circ}$  (CW phase). At 4.4 T the structure is incommensurate again and modulates between the W and V configuration (IVW phase) with opening of  $\approx 85^{\circ}$ . The latter incommensurate configuration is also referred to as a fan phase [44].

#### E. Spin model Hamiltonian

The localized magnetic moments in Na<sub>2</sub>BaMn(PO<sub>4</sub>)<sub>2</sub> form a triangular lattice in the *ab* plane, with a Mn-Mn stacking along the *c* axis as described in Sec. III D. The phase diagrams and the spin structure discussed previously indicate the dynamics of a frustrated antiferromagnetic triangular lattice [14,41]. Initially, for Na<sub>2</sub>BaMn(PO<sub>4</sub>)<sub>2</sub> we considered a two-dimensional (2D) nearest-neighbor-only classical Heisenberg model with  $J_1 = -0.11$  meV and S = 5/2. The significant single-ion anisotropy of Mn<sup>+2</sup> ions points to an easy-axis anisotropy in the system. In order to reproduce the plateau in the reported magnetization measurements as a function of applied fields along the *c* axis [14],  $k^c = 0.035$  meV was added to our model Hamiltonian (see Fig. 6). Our first attempt to reproduce the experimental results

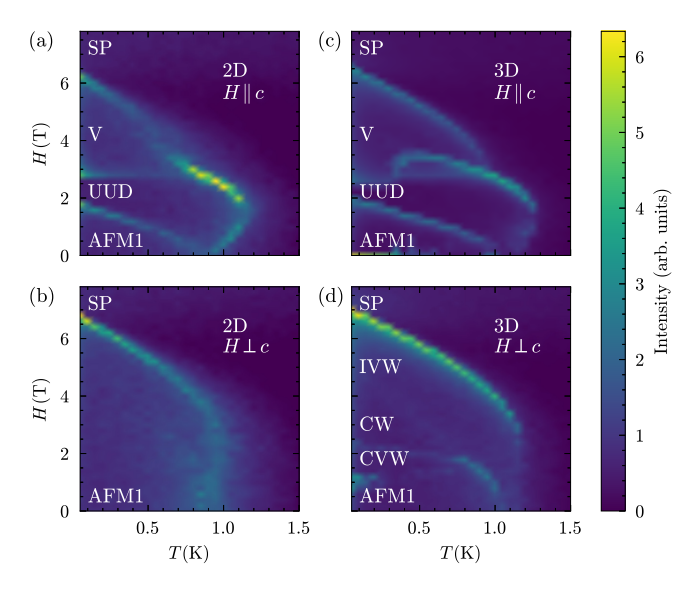


FIG. 7. Color maps of the calculated specific heat as a function of applied magnetic field and temperature for the (a), (b) 2D model and (c), (d) 3D model.

with this simple model is justified by the fact that two successive magnetic transitions at zero magnetic field are reported in other 2D triangular-lattice easy-axis AFM with high spin number [21,38,45].

The Monte Carlo simulations with this 2D model resulted in the color maps of the specific heat as a function of temperature and applied field, which are shown in Figs. 7(a) and 7(b). These heat maps reveal the boundaries between the different phases of the model. At finite temperatures and in zero field, a temperature separation of  $\sim 0.05$  K is observed between the AFM1 and AFM2 phases and the system becomes paramagnetic at  $\sim 0.95$  K. When the field is applied along the easy axis c, we identify at least four regions of the phase-space diagram in Fig. 7(a). Through spin dynamics simulations, we determined the spin configuration in each phase at zero temperature. AFM1: the ground state at zero field corresponds to a noncollinear 120° spin configuration where one of the three spins in the magnetic unit cell points along the easy axis (out of plane). UUD: at 2 T, the system displays a collinear up-up-down spin configuration. V: this phase resembles the UUD state, although it is noncollinear and it is marked by the rotations of the down spin towards the direction of the applied field. SP: at 6 T, the Zeeman energy dominates the exchange interactions and spin polarizes the system. In contrast, when the field is applied in plane, only two regions (AFM1 and SP) are distinguishable through the specific heat color map, as shown in Fig. 7(b). Starting from the ground state at zero field, when the external field dominates the single-ion anisotropy, one spin starts to point parallel to the field. At 3 T, we observe that two spins are perpendicular to the field, antiparallel to each other, but aligned along the easy axis, while the third spin remains parallel to the applied field. For higher fields, all spins continuously align with the field until the spin-polarized state is reached, slightly below 7 T. This phase sequence is consistent with the classical easy-axis triangular-lattice Heisenberg model [41].

This simple 2D model already seems to capture some features and the overall shape of the experimentally determined phase diagrams. It is important to mention that the experimental phase diagrams shown in Fig. 4 were obtained from a combination of neutron diffraction and specific heat measurements, while the theoretical phase diagrams were determined from the specific heat results from Monte Carlo simulations. Therefore, it is possible that the specific heat will not reveal all the field-induced transitions between the different phases. In addition, neutron diffraction data suggest that the magnetic order is characterized by an incommensurate wave vector along the c axis, as shown in Figs. 2 and 3, indicating that  $Na_2BaMn(PO_4)_2$  is a three-dimensional (3D) easy-axis antiferromagnet with considerable interlayer couplings. This corresponds to a spin configuration based on the 120° state, which offers a global rotation from one layer to the next. It is also worth mentioning that, based on Fig. 3(b), at zero field intense magnetic Bragg peaks are observed at positions with magnetic propagation vectors  $\mathbf{k} = (1/3, 1/3, \pm k_z)$ . Propagation vectors of this form have been attributed to frustrated interlayer couplings and are reported in compounds with stacked magnetic triangular layers such as the isostructural  $RbFe(MoO_4)_2$  [46].

In order to include the interaction between layers in our model, we attempted to reproduce the spiraling spin configuration in Na<sub>2</sub>BaMn(PO<sub>4</sub>)<sub>2</sub> via a frustration induced by two interlayer couplings. While the frustration 3D-coupling model was recently proposed for Na<sub>2</sub>BaCo(PO<sub>4</sub>)<sub>2</sub> [37], our study applies it to Na<sub>2</sub>BaMn(PO<sub>4</sub>)<sub>2</sub>, demonstrating its relevance also for S = 5/2 systems. It is based on the competition between  $J_2$ ,  $J_a$ , and  $J_b$ ; see Fig. 1(d). According to this model, the propagation vector along c is given by [37]

$$\tan(2\pi k_z) = \frac{3\sqrt{3}(J_b - J_a)}{3(J_b + J_a) - 2J_2}.$$
 (2)

In the  $P\bar{3}m1$  structure,  $J_a$  and  $J_b$  are equal by symmetry; however, if the system's crystal structure is  $P\bar{3}$ , thus losing a vertical mirror symmetry,  $J_a$  and  $J_b$  become independent of each other. The competition between pairs  $J_a$  and  $J_b$  or  $J_{a(b)}$  and  $J_2$  is enough to form the observed spin spiral due to frustration. Our simulations indicate that the  $J_a$ - $J_2$  model results in a better description of the experimental phase diagrams presented in Fig. 4. We determined that  $J_a = -0.0013$  and  $J_2 = -0.002$  meV (1-2% of  $J_1$ ) reproduce a propagation vector and roughly the phase boundaries of the field-temperature phase diagrams.

The resulting ground state spin configuration matches very well the experimentally determined one, with the exception that the model has a commensurable wavelength of five layers to allow for technical simplifications of the simulations. The specific-heat phase diagram for field out of plane is shown in Fig. 7(c), which is very similar to the 2D case, except for a new pocket created between the UUD and V phases. We note that at 2 T, with the 3D coupling, the spin configuration is similar to the up-up-down state. For a field in plane, while the 2D model only featured a single ordered phase, the 3D coupling introduced several phase boundaries to the diagram, although some of them are very faint, as seen in Fig. 7(d). It is worth mentioning that the 3D model results in ~0.18 K

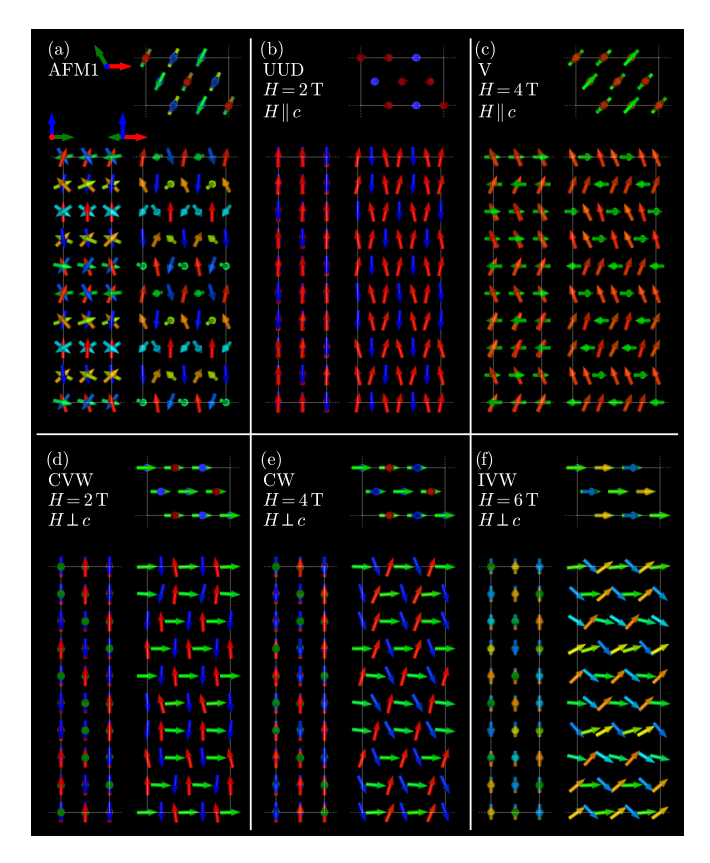


FIG. 8. Spin arrangements in the different phases based on the 3D model at  $T=0~\rm K$  for (a) the ground state, (b),(c) for external field applied out of plane, i.e., along the c axis, and (d)–(f) in plane, i.e., along the a axis.

separation between the two successive zero-field magnetic transitions and the paramagnetic state is observed at  $\sim\!1.18$  K. The evolution of the spin configurations for the two applied field directions at zero temperature is also displayed in Fig. 8 and a further comparison between the simulated and experimentally determined magnetic structures is presented in detail in the Supplemental Material (see Fig. S3 [43]). At this stage a perfect agreement between the experimentally determined magnetic structures and the theoretically obtained ones cannot be achieved; however, several features are captured by the proposed 3D model.

Detailed inelastic neutron scattering studies on single crystals for both field directions and additional theoretical modeling would be crucial to determine the Hamiltonian of the Na<sub>2</sub>BaMn(PO<sub>4</sub>)<sub>2</sub> system. Such measurements have been used to determine the microscopic Hamiltonian in the analog RbFe(MoO<sub>4</sub>)<sub>2</sub> [47], which also exhibits Y, UUD, and V phases and field-induced incommensurate stacking along the c axis [48]. For example, an alternative scenario might involve an Ising-like XXZ Hamiltonian where (i) the width of the 1/3 UUD plateau in Fig. 4(a) will depend on the XXZ exchange anisotropy of the  $J_1$  bond and (ii) the separation between the two zero-field transitions reported at 1.13 and 1.28 K will rely on the XXZ nature and on the 3D couplings [49].

Our reported *H-T* phase diagrams in Na<sub>2</sub>BaMn(PO<sub>4</sub>)<sub>2</sub> largely follow the archetypal frustrated triangular-lattice antiferromagnet scenario (coplanar Y and V phases separated by

the UUD state) as summarized in Ref. [50]. A key difference from the strictly 2D picture is that the propagation vector acquires a field-tunable out-of-plane component,  $k_z(H, T) \neq 0$ , which signals weak and frustrated interlayer exchange and is captured by our minimal 3D model. We also note that the very low-field region of the TLA phase diagram is explicitly flagged as unsettled in Ref. [50] and is where we capture the AFM2 phase. Its character, i.e., a longitudinal (easy-axis) ordering that precedes the coplanar AFM1 on cooling, is consistent with the XXZ triangular model in the presence of weak easy-axis anisotropy and weak 3D coupling and with theoretical expectations for zero field [51]. Within this context,  $RbFe(MoO_4)_2$  realizes the canonical Y-UUD-V sequence with commensurate stacking for field applied in plane [48], whereas in CuCrO<sub>2</sub> weak interlayer couplings and easy-axis anisotropy drive incommensurate stacking and a rich fieldinduced cascade [52,53]; see also Ref. [54] for the crucial role of interlayer exchange in the incommensurate phases. In Na<sub>2</sub>BaMn(PO<sub>4</sub>)<sub>2</sub>, the combination of easy-axis anisotropy and frustrated interlayer exchange could explain both the evolution  $k_z \neq 0$  in applied field and the finite zero-field AFM2 pocket.

#### IV. CONCLUSIONS

To conclude, we have reported detailed heat capacity, x-ray, and neutron diffraction measurements in single crystals of the S = 5/2 triangular-lattice antiferromagnet Na<sub>2</sub>BaMn(PO<sub>4</sub>)<sub>2</sub>. Based on x-ray diffraction refinements, the crystal structure exhibits subtle distortions that break the vertical mirror planes of the trigonal symmetry and reduce the space group from  $P\bar{3}m1$  to  $P\bar{3}$ . Heat capacity and neutron diffraction measurements under magnetic fields applied along the c axis and in the ab plane allowed us to identify several field-induced transitions in the temperature and magnetic field phase diagrams. We refined the magnetic structures of Na<sub>2</sub>BaMn(PO<sub>4</sub>)<sub>2</sub> according to the representation analysis of the modulation vector  $\mathbf{k} = (1/3, 1/3, k_7)$ , where the component  $k_z$  changes with magnetic field. In the ground state, the out-of-plane incommensurate component  $k_z$  of the propagation vector indicates non-negligible interlayer couplings. By employing a classical Heisenberg Hamiltonian that includes a single-ion anisotropy term ( $k^c = 0.035 \text{ meV}$ ), nearest-neighbor interactions in plane ( $J_1 = -0.11 \text{ meV}$ ), and interlayer couplings ( $J_a = -0.0013$  and  $J_2 = -0.002$  meV), and in combination with Monte Carlo simulations, we reproduced several features in the reported phase diagrams and the spin structures. Our data and simulations show that Na<sub>2</sub>BaMn(PO<sub>4</sub>)<sub>2</sub> is far more three-dimensionally coupled than assumed and that a minimal frustrated interlayer Heisenberg model captures the main features of its rich field-induced phase diagram.

#### ACKNOWLEDGMENTS

We acknowledge help from N. Qureshi for Mag2POL and from O. Fabelo for the initial x-ray single crystal diffraction measurements performed at ILL. We thank B. Normand and A. M. Läuchli for discussions and comments. This work was supported by the Czech Science Foundation GAČR under

the Junior Star Grant No. 21-24965M (MaMBA), by the Czech Ministry of Education Youth and Sports Grant No. LUABA24056 (BaCQuERel), and by the NCCR MARVEL, a National Centre of Competence in Research, funded by the Swiss National Science Foundation (Grant No. 205602). Crystals were grown and characterized in MGML (mgml.eu),

which is supported within the program of Czech Research Infrastructures (Project No. LM2023065).

#### DATA AVAILABILITY

The data that support the findings of this article are openly available [55–57]; embargo periods may apply.

- [1] L. Savary and L. Balents, Quantum spin liquids: A review, Rep. Prog. Phys. **80**, 016502 (2017).
- [2] L. Balents, Spin liquids in frustrated magnets, Nature (London) 464, 199 (2010).
- [3] C. Broholm, R. J. Cava, S. A. Kivelson, D. G. Nocera, M. R. Norman, and T. Senthil, Quantum spin liquids, Science 367, eaay0668 (2020).
- [4] X. G. Wen, Mean-field theory of spin-liquid states with finite energy gap and topological orders, Phys. Rev. B 44, 2664 (1991).
- [5] M. F. Collins and O. A. Petrenko, Review/synthése: Triangular antiferromagnets, Can. J. Phys. 75, 605 (1997).
- [6] J. Tapp, C. R. dela Cruz, M. Bratsch, N. E. Amuneke, L. Postulka, B. Wolf, M. Lang, H. O. Jeschke, R. Valentí, P. Lemmens, and A. Möller, From magnetic order to spin-liquid ground states on the  $s=\frac{3}{2}$  triangular lattice, Phys. Rev. B **96**, 064404 (2017).
- [7] S. Lee, R. Klauer, J. Menten, W. Lee, S. Yoon, H. Luetkens, P. Lemmens, A. Möller, and K.-Y. Choi, Unconventional spin excitations in the  $S = \frac{3}{2}$  triangular antiferromagnet RbAg<sub>2</sub>Cr[VO<sub>4</sub>]<sub>2</sub>, Phys. Rev. B **101**, 224420 (2020).
- [8] M. Matsuda, M. Azuma, M. Tokunaga, Y. Shimakawa, and N. Kumada, Disordered ground state and magnetic field-induced long-range order in an S=3/2 antiferromagnetic honeycomb lattice compound  ${\rm Bi_3Mn_4O_{12}(NO_3)}$ , Phys. Rev. Lett. **105**, 187201 (2010).
- [9] M. Lee, E. S. Choi, X. Huang, J. Ma, C. R. Dela Cruz, M. Matsuda, W. Tian, Z. L. Dun, S. Dong, and H. D. Zhou, Magnetic phase diagram and multiferroicity of Ba<sub>3</sub>MnNb<sub>2</sub>O<sub>9</sub>: A spin-<sup>5</sup>/<sub>2</sub> triangular lattice antiferromagnet with weak easy-axis anisotropy, Phys. Rev. B 90, 224402 (2014).
- [10] H. D. Rosales, D. C. Cabra, C. A. Lamas, P. Pujol, and M. E. Zhitomirsky, Broken discrete symmetries in a frustrated honeycomb antiferromagnet, Phys. Rev. B 87, 104402 (2013).
- [11] L. Seabra, P. Sindzingre, T. Momoi, and N. Shannon, Novel phases in a square-lattice frustrated ferromagnet: <sup>1</sup>/<sub>3</sub>magnetization plateau, helicoidal spin liquid, and vortex crystal, Phys. Rev. B 93, 085132 (2016).
- [12] R. Zhong, S. Guo, G. Xu, Z. Xu, and R. J. Cava, Strong quantum fluctuations in a quantum spin liquid candidate with a Co-based triangular lattice, Proc. Natl. Acad. Sci. USA 116, 14505 (2019).
- [13] N. Li, Q. Huang, A. Brassington, X. Y. Yue, W. J. Chu, S. K. Guang, X. H. Zhou, P. Gao, E. X. Feng, H. B. Cao, E. S. Choi, Y. Sun, Q. J. Li, X. Zhao, H. D. Zhou, and X. F. Sun, Quantum spin state transitions in the spin-1 equilateral triangular lattice antiferromagnet Na<sub>2</sub>BaNi(PO<sub>4</sub>)<sub>2</sub>, Phys. Rev. B 104, 104403 (2021).

- [14] J. Kim, K. Kim, E. Choi, Y. Joon Ko, D. Woo Lee, S. Ho Lim, J. Hoon Jung, and S. Lee, Magnetic phase diagram of a 2-dimensional triangular lattice antiferromagnet Na<sub>2</sub>BaMn(PO<sub>4</sub>)<sub>2</sub>, J. Phys.: Condens. Matter 34, 475803 (2022).
- [15] J. Xiang, C. Zhang, Y. Gao, W. Schmidt, K. Schmalzl, C.-W. Wang, B. Li, N. Xi, X.-Y. Liu, H. Jin, G. Li, J. Shen, Z. Chen, Y. Qi, Y. Wan, W. Jin, W. Li, P. Sun, and G. Su, Giant magnetocaloric effect in spin supersolid candidate Na<sub>2</sub>BaCo(PO<sub>4</sub>)<sub>2</sub>, Nature (London) 625, 270 (2024).
- [16] Y. Gao, Y.-C. Fan, H. Li, F. Yang, X.-T. Zeng, X.-L. Sheng, R. Zhong, Y. Qi, Y. Wan, and W. Li, Spin supersolidity in nearly ideal easy-axis triangular quantum antiferromagnet Na<sub>2</sub>BaCo(PO<sub>4</sub>)<sub>2</sub>, npj Quantum Mater. 7, 89 (2022).
- [17] J. Sheng, L. Wang, A. Candini, W. Jiang, L. Huang, B. Xi, J. Zhao, H. Ge, N. Zhao, Y. Fu, J. Ren, J. Yang, P. Miao, X. Tong, D. Yu, S. Wang, Q. Liu, M. Kofu, R. Mole, G. Biasiol et al., Two-dimensional quantum universality in the spin-1/2 triangular-lattice quantum antiferromagnet Na<sub>2</sub>BaCo(PO<sub>4</sub>)<sub>2</sub>, Proc. Natl. Acad. Sci. USA 119, e2211193119 (2022).
- [18] J. Sheng, J.-W. Mei, L. Wang, X. Xu, W. Jiang, L. Xu, H. Ge, N. Zhao, T. Li, A. Candini, B. Xi, J. Zhao, Y. Fu, J. Yang, Y. Zhang, G. Biasiol, S. Wang, J. Zhu, P. Miao, X. Tong *et al.*, Bose–Einstein condensation of a two-magnon bound state in a spin-1 triangular lattice, Nat. Mater. 24, 544 (2025).
- [19] Q. Huang, H. Zhang, Y. Hao, W. Yao, D. M. Pajerowski, A. A. Aczel, E. S. Choi, K. Barros, B. Normand, H. Zhou, A. M. Läuchli, X. Bai, and S.-S. Zhang, Universal dynamics of a pair condensate, arXiv:2503.13609.
- [20] N. Li, Q. Huang, X. Y. Yue, W. J. Chu, Q. Chen, E. S. Choi, X. Zhao, H. D. Zhou, and X. F. Sun, Possible itinerant excitations and quantum spin state transitions in the effective spin-1/2 triangular-lattice antiferromagnet Na<sub>2</sub>BaCo(PO<sub>4</sub>)<sub>2</sub>, Nat. Commun. 11, 4216 (2020).
- [21] H. Kitazawa, H. Suzuki, H. Abe, J. Tang, and G. Kido, High-field magnetization of triangular lattice antiferromagnet: GdPd<sub>2</sub>Al<sub>3</sub>, Phys. B: Condens. Matter 259-261, 890 (1999).
- [22] L. E. Svistov, A. I. Smirnov, L. A. Prozorova, O. A. Petrenko, A. Micheler, N. Büttgen, A. Y. Shapiro, and L. N. Demianets, Magnetic phase diagram, critical behavior, and two-dimensional to three-dimensional crossover in the triangular lattice antiferromagnet RbFe(MoO<sub>4</sub>)<sub>2</sub>, Phys. Rev. B 74, 024412 (2006).
- [23] C. Zhang, J. Xiang, C. Su, D. Sheptyakov, X. Liu, Y. Gao, P. Sun, W. Li, G. Su, and W. Jin, Successive magnetic transitions in the spin-<sup>5</sup>/<sub>2</sub> easy-axis triangular-lattice antiferromagnet Na<sub>2</sub>BaMn(PO<sub>4</sub>)<sub>2</sub>: A neutron diffraction study, Phys. Rev. B 110, 214405 (2024).
- [24] Agilent, CrysAlis<sup>Pro</sup> software system, ver. 1.171.36.28 (Agilent Technologies UK Ltd., Oxford, UK, 2013).

- [25] G. M. Sheldrick, A short history of SHELX, Acta Crystallogr., A 64, 112 (2008).
- [26] A. Scheie, LongHCPulse: Long-pulse heat capacity on a quantum design PPMS, J. Low Temp. Phys. 193, 60 (2018).
- [27] E. Ressouche, J. Chiapusio, B. Longuet, F. Mantegazza, and J. Flouquet, The new thermal-neutron diffractometer D23, ILL Tech. Rep. 123, 92 (1999).
- [28] N. Qureshi, *Mag2Pol*: A program for the analysis of spherical neutron polarimetry, flipping ratio and integrated intensity data, J. Appl. Crystallogr. **52**, 175 (2019).
- [29] G. P. Müller, M. Hoffmann, C. Dißelkamp, D. Schürhoff, S. Mavros, M. Sallermann, N. S. Kiselev, H. Jónsson, and S. Blügel, Spirit: Multifunctional framework for atomistic spin simulations, Phys. Rev. B 99, 224414 (2019).
- [30] F. J. dos Santos, M. dos Santos Dias, F. S. M. Guimarães, J. Bouaziz, and S. Lounis, Spin-resolved inelastic electron scattering by spin waves in noncollinear magnets, Phys. Rev. B 97, 024431 (2018).
- [31] R. F. L. Evans, W. J. Fan, P. Chureemart, T. A. Ostler, M. O. A. Ellis, and R. W. Chantrell, Atomistic spin model simulations of magnetic nanomaterials, J. Phys.: Condens. Matter 26, 103202 (2014).
- [32] VAMPIRE software package version 6.0.0 available from https: //vampire.york.ac.uk (Version 4c9651daecc86c3e6b6df0c8055 fcd9e89fd900c).
- [33] Y. Kajita, T. Nagai, S. Yamagishi, K. Kimura, M. Hagihala, and T. Kimura, Ferroaxial transitions in glaserite-type  $Na_2BaM(PO_4)_2$  (M = Mg, Mn, Co, and Ni), Chem. Mater. 36, 7451 (2024).
- [34] D. Nishio-Hamane, T. Minakawa, and H. Okada, Iwateite, Na<sub>2</sub>BaMn(PO<sub>4</sub>)<sub>2</sub>, a new mineral from the Tanohata mine, Iwate prefecture, Japan, J. Mineral. Petrol. Sci. **109**, 34 (2014).
- [35] C. Zhang, J. Xiang, Q. Zhu, L. Wu, S. Zhang, J. Xu, W. Yin, P. Sun, W. Li, G. Su, and W. Jin, Structural, magnetic, and magnetocaloric properties of triangular-lattice transition-metal phosphates, Phys. Rev. Mater. 8, 044409 (2024).
- [36] G. Nénert, M. M. Murshed, T. B. Hamed, T. M. Gesing, and M. B. Amara, Crystal structure of the synthetic analog of iwateite, Na<sub>2</sub>BaMn(PO<sub>4</sub>)<sub>2</sub>: An X-ray powder diffraction and Raman study, Z. Kristallogr. - Cryst. Mater. 235, 433 (2020).
- [37] L. Woodland, R. Okuma, J. R. Stewart, C. Balz, and R. Coldea, From continuum excitations to sharp magnons via transverse magnetic field in the spin-½ Ising-like triangular lattice antiferromagnet Na<sub>2</sub>BaCo(PO<sub>4</sub>)<sub>2</sub>, Phys. Rev. B **112**, 104413 (2025).
- [38] R. Ishii, S. Tanaka, K. Onuma, Y. Nambu, M. Tokunaga, T. Sakakibara, N. Kawashima, Y. Maeno, C. Broholm, D. P. Gautreaux, J. Y. Chan, and S. Nakatsuji, Successive phase transitions and phase diagrams for the quasi-two-dimensional easyaxis triangular antiferromagnet Rb<sub>4</sub>Mn(MoO<sub>4</sub>)<sub>3</sub>, Europhys. Lett. 94, 17001 (2011).
- [39] J. Villain, R. Bidaux, J.-P. Carton, and R. Conte, Order as an effect of disorder, J. Phys. France 41, 1263 (1980).
- [40] C. L. Henley, Ordering due to disorder in a frustrated vector antiferromagnet, Phys. Rev. Lett. **62**, 2056 (1989).
- [41] L. Seabra, T. Momoi, P. Sindzingre, and N. Shannon, Phase diagram of the classical Heisenberg antiferromagnet on a triangular

- lattice in an applied magnetic field, Phys. Rev. B **84**, 214418 (2011).
- [42] D. Yamamoto, G. Marmorini, and I. Danshita, Quantum phase diagram of the triangular-lattice *XXZ* model in a magnetic field, Phys. Rev. Lett. **112**, 127203 (2014).
- [43] See Supplemental Material at http://link.aps.org/supplemental/ 10.1103/kszh-m6bf for supporting experimental and theoretical information.
- [44] T. Nagamiya, Helical spin ordering—1 theory of helical spin configurations, Solid State Physics 20, 305 (1968).
- [45] K. Kimura, H. Nakamura, K. Ohgushi, and T. Kimura, Magnetoelectric control of spin-chiral ferroelectric domains in a triangular lattice antiferromagnet, Phys. Rev. B 78, 140401 (2008).
- [46] A. J. Hearmon, F. Fabrizi, L. C. Chapon, R. D. Johnson, D. Prabhakaran, S. V. Streltsov, P. J. Brown, and P. G. Radaelli, Electric field control of the magnetic chiralities in ferroaxial multiferroic RbFe(MoO<sub>4</sub>)<sub>2</sub>, Phys. Rev. Lett. **108**, 237201 (2012).
- [47] J. S. White, C. Niedermayer, G. Gasparovic, C. Broholm, J. M. S. Park, A. Y. Shapiro, L. A. Demianets, and M. Kenzelmann, Multiferroicity in the generic easy-plane triangular lattice antiferromagnet RbFe(MoO<sub>4</sub>)<sub>2</sub>, Phys. Rev. B 88, 060409 (2013).
- [48] Y. A. Sakhratov, O. Prokhnenko, A. Y. Shapiro, H. D. Zhou, L. E. Svistov, A. P. Reyes, and O. A. Petrenko, High-field magnetic structure of the triangular antiferromagnet RbFe(MoO<sub>4</sub>)<sub>2</sub>, Phys. Rev. B 105, 014431 (2022).
- [49] H. Jia, B. Ma, Z. D. Wang, and G. Chen, Quantum spin supersolid as a precursory Dirac spin liquid in a triangular lattice antiferromagnet, Phys. Rev. Res. 6, 033031 (2024).
- [50] O. A. Starykh, Unusual ordered phases of highly frustrated magnets: a review, Rep. Prog. Phys. 78, 052502 (2015).
- [51] H. Kawamura, A. Yamamoto, and T. Okubo, Z<sub>2</sub>-Vortex ordering of the triangular-lattice Heisenberg antiferromagnet, J. Phys. Soc. Jpn. 79, 023701 (2010).
- [52] E. Mun, M. Frontzek, A. Podlesnyak, G. Ehlers, S. Barilo, S. V. Shiryaev, and V. S. Zapf, High magnetic field evolution of ferroelectricity in CuCrO<sub>2</sub>, Phys. Rev. B 89, 054411 (2014).
- [53] Y. A. Sakhratov, L. E. Svistov, P. L. Kuhns, H. D. Zhou, and A. P. Reyes, Magnetic phases of the quasi-two-dimensional antiferromagnet CuCrO<sub>2</sub> on a triangular lattice, Phys. Rev. B 94, 094410 (2016).
- [54] M. Frontzek, J. T. Haraldsen, A. Podlesnyak, M. Matsuda, A. D. Christianson, R. S. Fishman, A. S. Sefat, Y. Qiu, J. R. D. Copley, S. Barilo, S. V. Shiryaev, and G. Ehlers, Magnetic excitations in the geometrically frustrated multiferroic CuCrO<sub>2</sub>, Phys. Rev. B 84, 094448 (2011).
- [55] https://doi.ill.fr/10.5291/ILL-DATA.CRG-3064 (2024).
- [56] https://doi.ill.fr/10.5291/ILL-DATA.5-41-1252 (2024).
- [57] N. Biniskos, F. J. dos Santos, M. Stekiel, K. Schmalzl, E. Ressouche, D. Sviták, A. Labh, M. Vališka, N. Marzari, and P. Čermák, Reproducibility package for article: Spin structures and phase diagrams of the spin-5/2 triangular-lattice antiferromagnet Na<sub>2</sub>BaMn(PO<sub>4</sub>)<sub>2</sub> under magnetic field, Figshare, (2025), https://doi.org/10.6084/m9.figshare.29899553.v1.